Physics of Fluids LETTER pubs.aip.org/aip/pof

Bundle size selection in dynamic elastocapillary aggregation of elastic fins

Cite as: Phys. Fluids **38**, 071703 (2026); doi: 10.1063/5.0339975
Submitted: 21 April 2026 · Accepted: 7 July 2026 ·
Published Online: 20 July 2026

View Online Export Citation CrossMark

Chan Jin Park,[1] Youngsin Jo,[2] Seokmin Moon,[2] and Jonghyun Ha[2,a)]

AFFILIATIONS

[1]Department of Chemical and Biological Engineering, Princeton University, Princeton, New Jersey 08544, USA
[2]Department of Mechanical Engineering, Ajou University, Suwon, Gyeonggi-Do 16499, Republic of Korea

[a)]Author to whom correspondence should be addressed: hajh@ajou.ac.kr

ABSTRACT

Elastocapillary aggregation is studied under quasi-static conditions, yet many applications involve dynamic withdrawal from a liquid bath. Here, we show that withdrawal speed governs bundle formation in parallel elastic fin arrays. At low speeds, bundle size is independent of withdrawal speed. At higher speeds, a dynamic meniscus amplifies capillary forces and promotes larger bundles. At the highest speeds, the bundle size saturates at an upper limit set by the sample design. We introduce the dry length of formed bundles as a proxy for the dynamic meniscus height and develop a theoretical model predicting the equilibrium bundle size through an energy balance. The resulting scaling collapses all experimental data, establishing withdrawal speed as a tunable parameter for elastocapillary aggregation.

Published under an exclusive license by AIP Publishing. https://doi.org/10.1063/5.0339975

20 July 2026 09:29:22

Capillary forces arising from surface tension can deform elastic solids at small length scales, a phenomenon broadly termed elastocapillarity.[1–4] The intrinsic length scale governing the transition from elasticity-dominated to capillarity-dominated behavior is the elastocapillary length $l_{EC} = (B/\gamma)^{1/2}$, where B is the bending stiffness and γ is the surface tension.[1] When the characteristic structural length exceeds l_{EC}, capillary forces are sufficient to drive significant elastic deformation, making the structure susceptible to elastocapillary aggregation. Since the seminal studies on capillary-driven bending and coalescence of slender fibers and sheets immersed in liquid,[1,2,5] extensive effort has been devoted to understanding the interplay between surface and elastic energies at the micro- and nanoscales. These interactions govern a wide range of systems, including carbon nanotube forests,[6] biological hairs and bristles,[7–9] gecko-inspired dry adhesives,[10] and microfabricated pillar arrays.[11–14]

Given their ubiquity, elastocapillary interactions play a critical role in a range of industrial processes. During the drying of micro-electro-mechanical systems (MEMS), residual liquid bridges between neighboring microstructures can lead to structural collapse.[11,13] In dip-coating of fibrous materials, a scalable route to functional surface coatings for biomedical, optical, and energy applications,[15–18] capillary-induced aggregation during withdrawal produces nonuniform coatings that compromise device performance.[19,20] In the fabrication of hierarchical nanostructures via capillary-driven self-assembly, precise control of bundle size is essential to achieving the desired morphology.[21–23] In these applications, the ability to predict and control the degree of elastocapillary aggregation is of considerable practical importance.

Despite this relevance, most prior work has focused on quasi-static configurations in which capillary and elastic forces are assumed to be in mechanical equilibrium.[1,2,24,25] In contrast, dynamic cases, where the liquid interface evolves during active withdrawal,[26] have received relatively little attention, although dynamic effects in elastocapillary interactions have attracted increasing attention in recent years.[27–32] For example, the final bundle diameter of paintbrush-like structures depends on withdrawal speed through viscous entrainment.[30] Additionally, compared to the static case, the capillary force between two parallel fibers can increase by an order of magnitude under dynamic conditions due to the formation of a dynamic meniscus.[31] These findings indicate that dynamic effects can significantly alter the elastocapillary energy landscape. However, despite these advances, we still lack a predictive framework that connects dynamic meniscus formation with bundle size selection in arrays of structures.

Here, we address this gap by investigating the elastocapillary aggregation of parallel elastic fins during withdrawal from a liquid bath. We show that dynamic withdrawal introduces a distinct regime in which the bundle size is directly controlled by withdrawal speed through the formation of a dynamic meniscus whose height increases with speed. This leads to a transition from a quasi-static regime to a dynamic regime in which aggregation is significantly enhanced. We further show that this dynamic enhancement is bounded on both ends, by a quasi-static limit at low speeds and by a saturation limit at

Published under an exclusive license by AIP Publishing

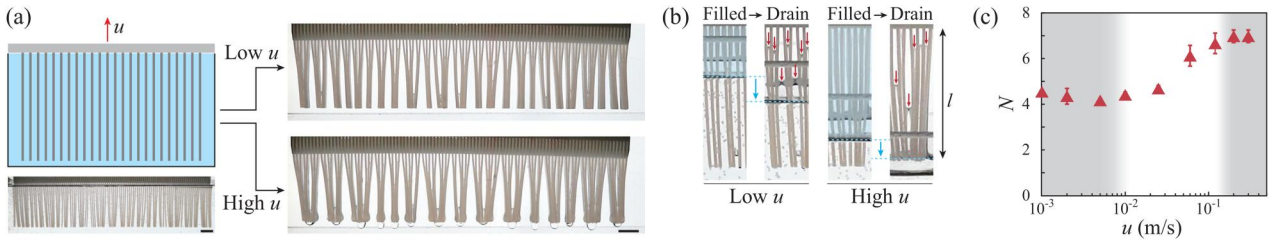


FIG. 1. Dynamic elastocapillary aggregation of parallel elastic fins. (a) Schematic of the withdrawal process and representative images of the fin array after withdrawal at low ($u = 0.001$ m/s, top) and high ($u = 0.12$ m/s, bottom) speeds. Larger bundles form at higher withdrawal speeds. Scale bars, 10 mm. (b) Images of menisci formed in the inter-fin gaps at low (left) and high u (right), captured at the same withdrawal height. The images illustrate the redistribution of the entrained liquid column, as the fins emerge from the bath. Taller menisci at higher u indicate suppressed drainage and increased liquid entrainment. Red arrows denote the menisci, and l is the fin length. (c) Experimentally measured average bundle size N as a function of u for $l = 40$ mm and $s = 1$ mm. The shaded regions denote the two limits of the dynamic regime. The left shaded region indicates the quasi-static regime ($u < u_c$), where N remains nearly constant, and the right shaded region indicates the saturation regime at high speeds, where dynamic effects no longer increase the bundle size. Above $u_c \approx 0.01$ m/s, N increases monotonically with u, demonstrating dynamic enhancement of elastocapillary aggregation. Error bars denote standard deviations.

high speeds set by the sample design. The dynamic meniscus height is captured experimentally through the dry length, defined as the contact-free portion of a bundle after aggregation, and the entrained liquid column height. We develop a scaling model based on viscous entrainment of liquid into the inter-fin gap to predict the dynamic meniscus height, and an energy-based model to predict the equilibrium bundle size. Theoretical predictions show quantitative agreement with experiments up to a constant prefactor of order unity. These results identify dynamic meniscus formation as the key mechanism governing elastocapillary aggregation and establish withdrawal speed as a tunable control parameter for the capillary-driven assembly of deformable solids.

Figure 1(a) shows the schematic of the withdrawal process with representative post-withdrawal images of the fin array at low (0.001 m/s) and high (0.12 m/s) withdrawal speeds, u. As the array is withdrawn, liquid menisci form between adjacent fins and exert lateral capillary forces that bend neighboring fins toward one another. When the capillary force exceeds the elastic restoring force of a fin, the fins coalesce into bundles.[1] We observe that the extent of aggregation depends strongly on u. At low u, predominantly small bundles consisting of 3–4 fins are formed, while at high u, substantially larger bundles consisting of 7–8 fins are observed. This trend indicates that dynamic effects during withdrawal control the size of the formed bundles.

To understand the physical origin of this velocity-dependent behavior, we examine the inter-fin menisci during withdrawal. Figure 1(b) shows the formation of menisci at low and high u, both captured at the same withdrawal height. As the fins are withdrawn from the bath, liquid is entrained between adjacent fins and subsequently redistributed into menisci.[30] At low u, the liquid has sufficient time to drain from the inter-fin gap under gravity, leaving only a short capillary meniscus and correspondingly weak lateral capillary forces. At high u, however, drainage is kinematically suppressed because the fin array rising faster than the liquid can drain through the narrow gap. Consequently, the entrained liquid column is substantially taller,[31] as indicated by the red arrows denoting the meniscus height in Fig. 1(b). Because a taller meniscus increases the total capillary interaction between adjacent fins,[33] the lateral attraction becomes stronger and promotes coalescence into larger bundles. The stark contrast between the two conditions provides clear evidence that the dynamic meniscus governs bundle size selection.

We measure the average bundle size N, which is defined as the total number of fins divided by the number of bundles formed after withdrawal. The dependence of N on u is shown in Fig. 1(c), where the fin length and inter-fin spacing are $l = 40$ mm and $s = 1$ mm, respectively. We observe two distinct regimes as a function of u. Below a critical speed $u_c \approx 0.01$ m/s, N is nearly independent of u, indicating a quasi-static regime (shaded in gray) in which the meniscus height is set by static capillary equilibrium, regardless of withdrawal speed. Above u_c, N increases monotonically with u, transitioning into a dynamic regime. For instance, increasing u from 0.01 to 0.3 m/s results in N growing from approximately 4 to 7, representing more than a 1.5-fold increase. At the highest speeds, however, the growth of N weakens, and the bundle size approaches a plateau, as indicated by the shaded region at high u in Fig. 1(c). This shows that the dynamic enhancement is itself bounded, and the physical origin of this upper limit is examined in detail later. These results demonstrate that withdrawal speed provides direct and quantitative control over elastocapillary aggregation.

Figure 2 illustrates the overall experimental setup and procedure. PDMS (polydimethylsiloxane) fins of width $w = 5$ mm and thickness $t = 1$ mm were fabricated by casting uncured PDMS (Sylgard 184, 10:1 base-to-crosslinker ratio by weight) into custom aluminum

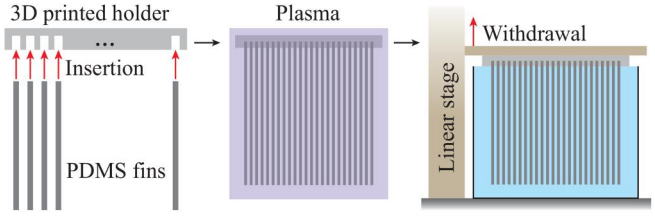


FIG. 2. Schematic of the experimental setup and procedure. The assembled fin array is treated with O_2 plasma to render the PDMS surfaces hydrophilic and then vertically immersed in a liquid bath. The array is subsequently withdrawn at a constant speed u using a motorized linear stage. The process is recorded with a camera for subsequent image analysis.

20 July 2026 09:29:22

Published under an exclusive license by AIP Publishing

molds, followed by thermal curing at 80 °C for 2 h. After demolding, the fins were cut to three different lengths, $l = 40$, 60, and 80 mm. The Young's modulus of the cured PDMS was independently measured by uniaxial tensile testing to be $E \approx 1.25$ MPa, giving a bending stiffness $B = Ewt^3/12 \approx 5 \times 10^{-7}$ N m^2, where w and t are the fin width and thickness, respectively. A total of 100 fins were mounted in parallel on a 3D-printed holder at two inter-fin spacings of $s = 0.5$ and 1 mm.

Prior to each experiment, the assembled fin array was treated with O_2 plasma (60 W, 60 s) to render PDMS surfaces hydrophilic, reducing the water contact angle to below 10° and eliminating contact angle hysteresis as a confounding variable. Plasma treatment was performed immediately before each experiment to ensure a consistent and reproducible initial wetting state. The treated array was then vertically immersed in either de-ionized water ($\rho = 998$ kg/m^3, $\mu = 1$ mPa s, and $\gamma = 72$ mN/m) or 80 wt. % aqueous glycerol solution ($\rho = 1208$ kg/m^3, $\mu = 32$ mPa s, and $\gamma = 67$ mN/m). Since aqueous glycerol solutions are hygroscopic, and their viscosity is sensitive to temperature and water content, the viscosity of the working solution was measured directly with a rotational rheometer (MCR702e, Anton Paar), and the solution behaved as a Newtonian fluid over the examined shear-rate range. After a short equilibration period of ~30 s to ensure complete and uniform wetting of all fin surfaces, the holder was withdrawn vertically at a constant speed u, ranging from 0.001 to 0.3 m/s, using a motorized linear stage. The withdrawal process was recorded with a camera, and the post-withdrawal images were analyzed using ImageJ.[34] Each experimental condition, defined by a unique combination of u, l, and s, was repeated at least three times to assess reproducibility, and results are reported as mean ± standard deviation.

During withdrawal, the dynamic meniscus leaves a clear geometric signature on the formed bundles, and we exploit this geometry to introduce the dry length, l_d, as a quantitative proxy for the dynamic meniscus height h. Unlike direct imaging of the inter-fin meniscus, which requires time-resolved optical access to the narrow gap between deforming fins, l_d can be measured unambiguously from a single post-withdrawal photograph using standard image analysis. This makes l_d a practical measure of the dynamic wetting state that is applicable across all experimental conditions, including dense fin arrays where *in situ* visualization is inherently limited.

As shown in Fig. 3(a), l_d is defined as the vertical extent of the upper dry portion of a fully formed bundle, measured from the top of the last liquid bridge to the clamped base of the fins. Physically, l_d corresponds to the length of fin that had already emerged above the liquid surface at the moment when capillary-driven aggregation was completed. The complementary length, $l - l_d$, therefore represents the span of fin over which the dynamic meniscus was actively driving coalescence during withdrawal. Smaller l_d indicates that aggregation was completed early in the withdrawal stroke, when only a short segment of the fins had emerged from the liquid bath, while larger l_d implies that coalescence continued until the fins were nearly fully extracted.

The inverse relationship between h and l_d is illustrated schematically in Fig. 3(b) and follows directly from the physics of meniscus-driven aggregation. At low u, viscous drainage efficiently removes liquid from the inter-fin gap as the array is withdrawn, keeping the meniscus short (small h). The resulting capillary force is weak and insufficient to recruit distant fins, so aggregation is completed only after a large fraction of the fin length has emerged from the bath, yielding a large l_d. At high u, by contrast, the fin array rises faster than the liquid can drain, entraining a substantially taller meniscus (large h). The amplified capillary force then drives rapid coalescence early in the withdrawal process, before much of the fin has emerged, leaving only a short dry region and hence a small l_d. This monotonic, inverse correspondence between h and l_d suggests that measuring l_d provides a practical proxy for the dynamic meniscus height.

Figure 3(c) shows l_d as a function of individual bundle size N for representative withdrawal speeds $u = 0.001$, 0.12, and 0.3 m/s at both spacings ($s = 0.5$ and 1 mm). For a fixed N, l_d decreases monotonically with increasing u. For example, at $N = 6$ and $s = 1$ mm, l_d decreases from approximately 28 mm at $u = 0.001$ m/s to 18 mm at $u = 0.3$ m/s, confirming that a taller dynamic meniscus enables aggregation to occur over a shorter length of the fins. Larger bundles ($N > 10$ for $s = 1$ mm and $N > 15$ for $s = 0.5$ mm) are observed only at the highest speed ($u = 0.3$ m/s) because forming large bundles requires capillary forces strong enough to simultaneously bend many

20 July 2026 09:29:22

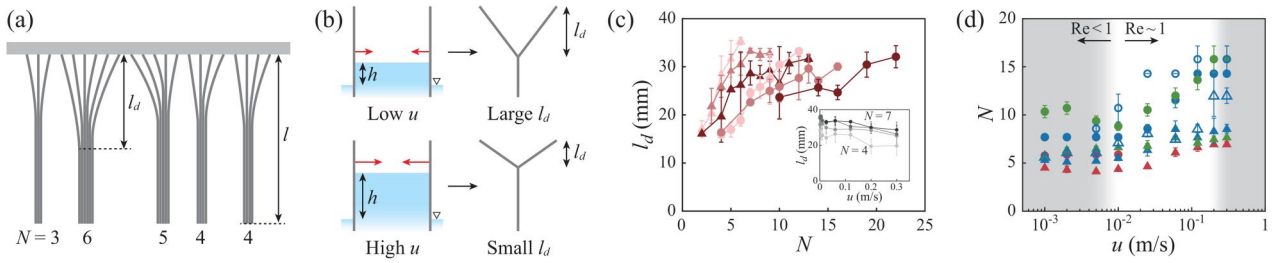


FIG. 3. Dry length as a proxy for dynamic meniscus height. (a) Schematic illustrating the definition of the dry length l_d. l and N denote the fin length and individual bundle size, respectively. The dry length is the vertical extent of the upper portion of a bundle, where adjacent fins are no longer connected by a liquid bridge. (b) Schematic illustrating the withdrawal and resulting l_d at low and high u. Due to the dynamic meniscus, a larger l_d is observed at low u and a smaller l_d at high u, indicating earlier aggregation at higher speeds. Black arrows denote the dynamic meniscus height. (c) Experimentally measured dry length l_d vs N for representative withdrawal speeds $u = 0.001$, 0.12, and 0.3 m/s at inter-fin spacings $s = 0.5$ and 1 mm. For a fixed N, l_d decreases with increasing u. Circles and triangles denote $s = 0.5$ and 1 mm, respectively, while darker colors indicate higher u. The inset shows l_d as a function of u for representative N ranging from 4 to 7, with darker lines corresponding to larger N. (d) Experimentally measured average bundle size N vs u for different fin lengths l and inter-fin spacings s. Circles and triangles denote $s = 0.5$ and 1 mm, respectively, while red, blue, and green denote $l = 40$, 60, and 80 mm, respectively. Filled and open symbols denote experiments conducted in de-ionized water and the glycerol solution, respectively. The shaded regions indicate the two limits of the dynamic regime. The left shaded region denotes the quasi-static regime (Re < 1), and the right shaded region denotes the saturation regime, in which dynamic effects no longer increase the bundle size.

Published under an exclusive license by AIP Publishing

fins, which, in turn, demands a sufficiently tall dynamic meniscus that is only achieved at high u.

At fixed N and u, l_d is consistently smaller for $s = 0.5$ mm than for $s = 1$ mm because closely spaced fins require less lateral deflection to bridge, reducing the elastic energy barrier and allowing aggregation to complete earlier during withdrawal, leaving a shorter dry region. The inset of Fig. 3(c) depicts l_d as a function of u for representative N of 4, 5, 6, and 7, showing that l_d remains nearly constant in the quasi-static regime ($u < 0.01$ m/s) but decreases monotonically with u in the dynamic regime for all bundle sizes. In addition, for fixed u, l_d increases with N, reflecting that larger bundles complete aggregation later during withdrawal. Taken together, these trends confirm that l_d encodes the dynamic meniscus height across experimental conditions.

We then measure the average bundle size N while independently varying u, l, and s. The results are summarized in Fig. 3(d), where two distinct regimes are consistently observed across all conditions. At low u, N is nearly independent of withdrawal speed, indicating a quasi-static regime (shaded in gray) in which inertial effects are negligible, and the bundle size is governed primarily by the static balance between capillary and elastic forces. At higher u, N increases monotonically with u, defining a dynamic regime in which the withdrawal speed directly controls the extent of aggregation through the formation of a taller dynamic meniscus. At sufficiently high u, however, N exhibits a gradual saturation, as indicated by the shaded region at high u in Fig. 3(d). This behavior arises because as the meniscus height increases, the elastic resistance to bending increases steeply with bundle size, and the additional capillary energy supplied by a taller meniscus eventually becomes insufficient to recruit further fins. The dynamic regime is therefore bounded on both ends. Once the sample design is fixed, that is, once the fin length l, the spacing s, the width w, and the bending stiffness B are specified, the bundle size converges to an intrinsic upper limit that cannot be exceeded, no matter how fast the array is withdrawn. This saturation limit is quantified by the theoretical model developed later. Regardless of the regime, N increases with l, as longer fins are more susceptible to capillary-driven deflection, and aggregation is more favorable at smaller s, where the lateral displacement required for coalescence is reduced. The transition between the two regimes consistently occurs near $u \approx 0.01$ m/s across all combinations of l and s.

We further characterize the experimental conditions using dimensionless numbers to identify the physical mechanisms at play. The capillary number $\mathrm{Ca} = \mu u/\gamma$ ranges from $O(10^{-4}$–$10^{-2})$, remaining well below unity across all conditions. This indicates that capillary stresses remain dominant relative to viscous stresses, and that capillarity is the primary driver of fin aggregation. The gap Reynolds number $\mathrm{Re} = \rho s u/\mu$, by contrast, spans a range that crosses unity within our experimental window. At low u, $\mathrm{Re} < 1$, and the flow in the inter-fin gap is purely viscous, allowing the meniscus to drain to its equilibrium height before the fins emerge from the bath. As u increases and Re approaches unity, inertial effects in the gap flow become significant. The liquid can no longer drain fast enough, and a dynamic meniscus is entrained. The coincidence of the quasi-static-to-dynamic transition with $\mathrm{Re} \sim 1$ identifies inertia as the key mechanism controlling the height of the dynamic meniscus: as the withdrawal speed increases beyond u_c, inertial effects suppress viscous drainage and sustain a taller meniscus between adjacent fins.

We now develop a theoretical model to rationalize the experimental results in the dynamic regime. We begin by constructing a model to predict the dynamic meniscus height h, which is the key variable controlling bundle size selection. When the fin array is withdrawn from the bath at speed u, the height of the liquid column entrained between adjacent fins is determined by the competition between liquid entrainment and viscous drainage. Liquid entrainment arises from the upward motion of the fins, which carries fluid along their surfaces and tends to sustain a tall meniscus. In contrast, viscous drainage is driven by gravity and pressure gradients, which induce flow through the narrow inter-fin gap and tend to reduce the meniscus height. The steady-state h is therefore set by the balance between these processes. At low u, viscous drainage dominates, and the meniscus approaches its equilibrium capillary height. At high u, liquid entrainment dominates, and a taller dynamic meniscus is sustained.

To estimate h, we consider the meniscus that spans the inter-fin gap, as illustrated in Fig. 4(a). In the quasi-static limit, a narrow gap ($s < l_c$, with $l_c = (\gamma/\rho g)^{1/2}$ the capillary length) holds liquid against gravity through the balance between the Laplace pressure γ/s and the hydrostatic pressure $\rho g h$, which sets the static scale $h \sim l_c^2/s$. During withdrawal, the moving fin walls entrain additional liquid by viscous drag, and a higher viscosity slows drainage from the gap and sustains a taller meniscus, as in the classical Landau–Levich entrainment.[35] This dynamic enhancement is governed by the capillary number $\mathrm{Ca} = \mu u/\gamma$, and a matching of the dynamic meniscus to the static gap curvature gives a dynamic correction that scales as a power of Ca. The meniscus height is therefore

$$h \sim \frac{l_c^2}{s}\,\mathrm{Ca}^{1/2} = \frac{l_c^2}{s}\left(\frac{\mu u}{\gamma}\right)^{1/2}, \tag{1}$$

where $\mathrm{Ca} = \mu u/\gamma$ is the capillary number. Equation (1) predicts $h \sim u^{1/2}$, so the meniscus grows as the square root of withdrawal speed, while the viscosity enters with a positive exponent, consistent with the physical expectation that a more viscous liquid is entrained more strongly. The prefactor l_c^2/s sets the absolute magnitude of the meniscus height and its dependence on the inter-fin spacing. The crossover from the quasi-static to the dynamic regime coincides with the onset of significant inertial effects near $\mathrm{Re} \sim 1$, where $\mathrm{Re} = \rho s u/\mu$ is the gap Reynolds number, in agreement with the experimentally observed onset near u_c.

To verify this prediction, we measured the height of the entrained liquid column just before the meniscus formation, as shown in Fig. 1(b). Since this liquid column redistributes into the dynamic menisci upon withdrawal, its height provides a direct estimate of h. As shown in Fig. 4(b), h is nearly independent of u in the quasi-static regime, consistent with capillary equilibrium, but increases with u in the dynamic regime. The dependence of h on the fin length l is weak, while arrays with smaller s exhibit larger h, both consistent with Eq. (1). A log–log plot of h vs u yields a slope of $1/2$, in quantitative agreement with the predicted scaling.

Having established how h is set by the withdrawal dynamics, we now consider how this meniscus drives fin aggregation. We begin by considering the meniscus geometry. When adjacent fins are bridged by a liquid column of height h, the meniscus spans the inter-fin gap s and wets the fin surface over h. The liquid meniscus bridging two adjacent fins separated by gap s acts as a capillary bridge under a Laplace pressure $\Delta P \sim \gamma/s$. This pressure acts over

20 July 2026 09:29:22

Published under an exclusive license by AIP Publishing

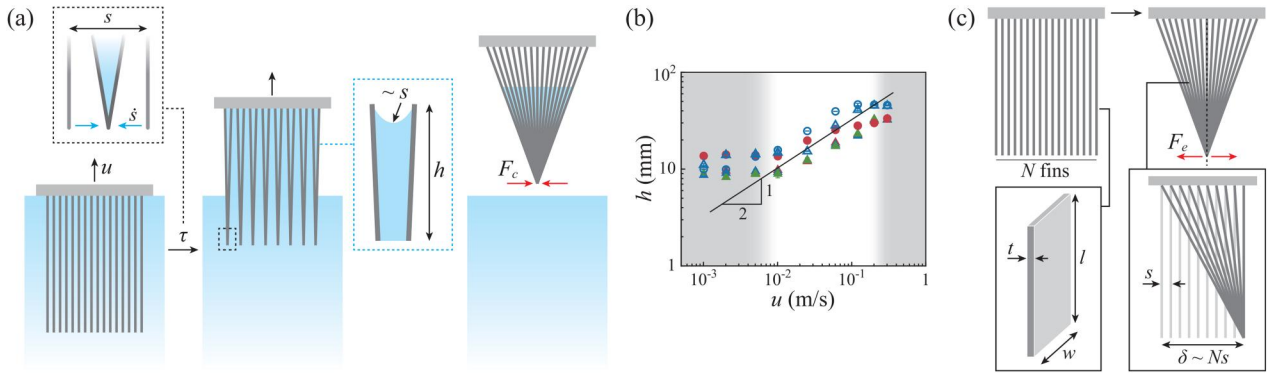


FIG. 4. Theoretical model for dynamic elastocapillary aggregation. (a) Schematic illustrating the model for the dynamic meniscus height h. The meniscus is modeled as a liquid column of height h between adjacent fins, where the steady-state height is governed by viscous liquid entrainment during withdrawal and capillary meniscus in the inter-fin gap. The black dashed box shows a magnified view of the inter-fin gap s, where the lateral deflection δ initiates coalescence. The blue dashed box shows a magnified view of the entrained liquid column of width $\sim s$ and height h that redistributes into the dynamic meniscus. (b) Measured entrained liquid column height h. The measured values follow a power law dependence on withdrawal speed with an exponent of 1/2. Circles and triangles denote $s = 0.5$ and 1 mm, respectively, while red, blue, and green symbols correspond to fin lengths $l = 40$, 60, and 80 mm, respectively. Filled and open symbols denote experiments conducted in de-ionized water and the glycerol solution, respectively. The shaded regions denote the quasi-static regime at low u and the saturation regime at high u, which bound the dynamic regime. (c) Schematic illustrating the energy-based model for bundle formation when N fins symmetrically coalesce into a bundle.

the effective wetted area wh on each fin, where w is the fin width, giving a lateral capillary force pulling the two fins together: $F_c \sim \Delta P \cdot wh \sim \gamma wh/s$. As illustrated in Fig. 4(a), F_c acts at the liquid bridge, pulling adjacent fins toward one another. This expression shows that F_c increases linearly with h, which is why a taller dynamic meniscus drives stronger aggregation at higher withdrawal speeds. We note that in our experiments, the contact angle is below 10° ($\cos\theta \approx 1$) due to O_2 plasma treatment, so the contact angle contributes only a numerical prefactor of order unity and does not affect the leading-order scaling.

To obtain the capillary energy, we integrate F_c over the displacement, through which two adjacent fins are brought together, which gives an energy of order γwh per liquid bridge. In a bundle of N fins, however, the inter-fin menisci on either side of an interior fin are of comparable height, and their capillary pulls nearly balance, since the liquid in all inter-fin gaps drains at a comparable rate during withdrawal. The net cohesive action that closes the bundle and selects its size therefore originates predominantly at the bundle boundary, where the meniscus is unbalanced, rather than from the sum of all interior bridges. The effective cohesive capillary energy is thus set by the boundary meniscus scale,

$$U_c \sim -\gamma wh, \tag{2}$$

independent of the number of fins N. The magnitude $|U_c|$ increases linearly with h, so a taller meniscus provides more cohesive capillary energy to drive aggregation, which is why N increases with u.

As the capillary force F_c pulls adjacent fins toward one another, each fin must bend laterally to accommodate the coalescence, resulting in an elastic restoring force that opposes further aggregation. For a single fin deflected by a distance δ at its free end, the elastic bending energy scales as $U_b \sim B\delta^2/l^3$. As illustrated in Fig. 4(c), when N fins symmetrically coalesce into a single bundle, the ith fin is displaced by $\delta_i \sim |i - (N+1)/2|\, s$ at its free end, meaning that fins farther from the bundle center must bend more. Summing the bending energy over all fins to leading order in N gives the total elastic energy

$$U_e \sim \sum_{i=1}^{N} \frac{B\delta_i^2}{l^3} \sim \frac{Bs^2}{l^3} N^3. \tag{3}$$

The cubic scaling $U_e \sim N^3$ is the consequence of the bundle geometry. Unlike a single deforming element where energy scales linearly with the number of structural units, each fin added to the periphery of the bundle must be deflected by a progressively larger displacement, so the marginal elastic energy cost grows as N^2, and the cumulative sum over all fins yields N^3. This superlinear growth of the elastic energy with the bundle size is the feature that limits aggregation, as the elastic resistance escalates rapidly as more fins are recruited into a bundle, eventually balancing the capillary driving force and setting the equilibrium bundle size.

A bundle of N fins is selected when the cohesive capillary energy that holds the bundle together becomes comparable to the elastic energy required to maintain the aggregated shape. Balancing the boundary-controlled cohesive energy $U_c \sim -\gamma wh$ from Eq. (2) against the elastic energy $U_e \sim Bs^2N^3/l^3$ from Eq. (3), that is, $\gamma wh \sim Bs^2N^3/l^3$, and solving for N gives the characteristic equilibrium bundle size

$$N \sim \left(\frac{\gamma\, w\, h\, l^3}{B\, s^2}\right)^{1/3}. \tag{4}$$

Equation (4) captures the trends observed in Fig. 3(d). N increases with h and l, as a taller meniscus supplies more cohesive capillary energy, and longer fins are more compliant to bending. In contrast, N decreases with B and s, since stiffer fins resist deflection more strongly, and wider spacing requires larger lateral displacements to bridge. The scaling $N \sim h^{1/3}$, combined with $h \sim u^{1/2}$ from Eq. (1), gives $N \sim u^{1/6}$ in the dynamic regime, consistent with the experimentally observed sub-linear growth of bundle size with withdrawal speed.

Equations (1) and (4) also delineate the range of withdrawal speeds, over which the dynamic enhancement operates. At the low speed end, for $\mathrm{Re} < 1$, viscous drainage keeps the meniscus at its

20 July 2026 09:29:22

Published under an exclusive license by AIP Publishing

capillary equilibrium height, so h and, hence, N are set by the static elastocapillary balance and are insensitive to u. At the high-speed end, the bundle size necessarily saturates. The dynamic meniscus height cannot exceed the fin length, $h \leq l$, so the cohesive capillary energy available to drive aggregation is bounded, and substituting $h_{\max} \sim l$ into Eq. (4) gives an intrinsic upper bound $N_{\max} \sim (\gamma w l^4/Bs^2)^{1/3}$. Across all fin lengths, spacings, and liquids examined, the measured plateau values agree with this bound up to an order-unity prefactor, supporting the proposed physical origin of the saturation. In addition, the marginal elastic cost of recruiting one more fin grows as N^2 because $U_e \sim N^3$, so the incremental capillary energy gained from a taller meniscus is eventually overwhelmed by the escalating bending penalty. Consequently, once the sample design is fixed, that is, once l, s, w, and B are specified, the bundle size converges to a design-limited value, and further increases in withdrawal speed leave N essentially unchanged. The proposed scaling law therefore describes the dynamic regime bounded by the quasi-static limit at low speeds and by the saturation limit at high speeds, consistent with the plateaus observed at both ends of Figs. 1(c) and 3(d).

We can rewrite Eq. (4) in dimensionless form by introducing the effective elastocapillary length $l_{\mathrm{EC}} = (B/\gamma w)^{1/2}$ and three dimensionless groups, which yields $N \sim (\eta\zeta\lambda)^{1/3}$. The first group, $\eta = l^2/l_{\mathrm{EC}}^2$, is the elastocapillary number, which measures how compliant the fin is relative to the elastocapillary length scale: a fin with $\eta \gg 1$ is long enough that capillary forces readily overcome its elastic resistance, promoting larger bundles. The second group, $\zeta = h/s$, is the dimensionless meniscus height, which encodes the effect of withdrawal dynamics. As u increases, h grows and ζ increases accordingly, directly amplifying the capillary driving force. The third group, $\lambda = l/s$, is the fin aspect ratio, which reflects the geometric susceptibility of the array to aggregation. Fins that are long relative to their spacing are more easily recruited into large bundles. This dimensionless form unifies the roles of material compliance (η), withdrawal dynamics (ζ), and fin geometry (λ) in a single compact expression, showing that increasing any one of these three groups promotes the formation of larger bundles.

We now validate the theoretical model by comparing its predictions with the experimental results, focusing on the dynamic regime where the withdrawal speed actively controls bundle size. For each experimental condition in this regime, h was obtained from Eq. (1) using the known fluid properties, and the theoretical bundle size N_{th} was computed from Eq. (4).

Figure 5(a) plots the experimentally measured mean bundle size N_{exp} against the theoretically predicted N_{th}, using a single constant prefactor of order unity. The data points from all combinations of l, s, and u follow the line of unit slope, demonstrating that the theoretical model correctly captures the overall trend of bundle size variation across all experimental conditions. The modest scatter about the line reflects higher-order effects such as geometric nonlinearity at large deflections and fin-to-fin variability in alignment, which are not captured by the leading-order scaling, and is consistent with the experimental run-to-run variability indicated by the error bars.

Figure 5(b) presents the same dataset in log–log form, plotting N_{exp} against the composite dimensionless group $\eta\zeta\lambda$. Despite the wide range of experimental conditions—spanning three fin lengths, two spacings, and nearly two decades in withdrawal speed—all data points collapse onto a single power law with a slope of 1/3, in agreement with the theoretical prediction $N \sim (\eta\zeta\lambda)^{1/3}$. This collapse is particularly significant because $\eta\zeta\lambda$ simultaneously encodes independent variations in l (which appears in both η and λ), s (which appears in both ζ and λ), and u (which enters through $\zeta = h/s \sim \mathrm{Ca}^{1/2}$), yet all of these variations are unified into a single power law with the predicted exponent. We acknowledge that the accessible parameter range in the present experiments limits the span of the scaling data to approximately one decade. The collapse of data from multiple independent parameter variations (u, l, and s) onto a single power law with the predicted exponent provides consistent support for the proposed scaling, and further experiments over an extended parameter range would be a valuable direction for future work. Taken together, Figs. 5(a) and 5(b) confirm that the dynamic meniscus height h, as predicted by Eq. (1), is the central quantity governing bundle size selection, and that the three dimensionless groups η, ζ, and λ correctly capture the combined roles of material compliance, fin geometry, and withdrawal dynamics in determining the equilibrium bundle size.

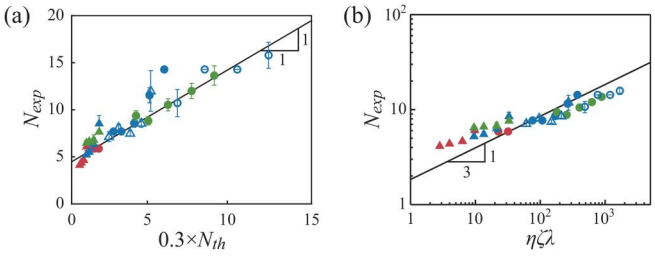


FIG. 5. Comparison between theoretical predictions and experimental results. (a) Experimentally measured average bundle size N_{exp} vs theoretically predicted bundle size N_{th} from Eq. (4). The solid line denotes a slope of 1. (b) Log–log plot of N_{exp} vs the product of the three dimensionless numbers $\eta\zeta\lambda$. The solid line denotes a slope of 1/3. The collapse of all data onto this power law confirms the universal scaling $N \sim (\eta\zeta\lambda)^{1/3}$ across all fin lengths, spacings, and withdrawal speeds. Circles and triangles denote $s = 0.5$ and 1 mm, respectively, while red, blue, and green markers correspond to fin lengths $l = 40$, 60, and 80 mm, respectively. Filled and open symbols denote experiments conducted in de-ionized water and the glycerol solution, respectively.

We have shown that the withdrawal speed of elastic fin arrays from a liquid bath provides quantitative control over elastocapillary aggregation. Two distinct regimes, a quasi-static regime at low withdrawal speeds, in which dynamic effects are negligible and the bundle size N is set by the static elastocapillary balance, and a dynamic regime at higher speeds, in which N increases monotonically with u and exceeds the quasi-static value by more than a factor of 1.5, were identified. At the highest speeds, the dynamic enhancement saturates and N converges to an upper limit set by the sample design, so the dynamic regime is bounded on both ends. The transition between these regimes occurs near $\mathrm{Re} = 1$, highlighting the key role of inertia in dynamic elastocapillary interactions. This enhanced aggregation arises from a taller dynamic meniscus formed between adjacent fins at higher withdrawal speeds, which amplifies capillary forces and drives coalescence into larger bundles.

We developed a theoretical model to capture the observed behavior. Based on a balance between viscous entrainment and capillary restoring forces, we first constructed a model to predict the dynamic meniscus height h. Using the obtained h and an energy

20 July 2026 09:29:22

Published under an exclusive license by AIP Publishing

balance between the cohesive capillary energy and the elastic energy, we developed a model for the equilibrium bundle size, which we further reduced by introducing three dimensionless groups. Experimental results were collapsed onto a single line with the theoretically predicted exponent, supporting the proposed scaling framework.

We introduced the dry length l_d of a formed bundle as a practically convenient proxy for the dynamic meniscus height. Since l_d can be measured from a post-withdrawal image, it provides a practical and accessible alternative to direct visualization of the dynamic meniscus, which is especially difficult in dense structures. However, when comparing structures of different lengths, the influence of the submerged portion should be considered, as longer fins tend to exhibit larger l_d due to their greater resistance to capillary-driven deformation.

We note that the present theoretical model is based on the Euler–Bernoulli beam theory under the small-deformation assumption. For the majority of experimental conditions, the lateral tip deflection satisfies $\delta/l \lesssim 0.1$, supporting the applicability of the present leading-order approximation. For the largest bundles at wide spacings, geometric nonlinearities may contribute higher-order corrections that are not captured by the present scaling framework, consistent with the modest scatter observed in Fig. 5(a) at large N.

The contact angle of water on the plasma-treated PDMS surface is below 10°, so that $\cos\theta \approx 1$. The contact angle therefore contributes only a numerical prefactor of order unity to the capillary energy and does not affect the leading-order scaling. Within the present scaling framework, increasing wettability (smaller contact angle) raises $\cos\theta$ and the equilibrium meniscus height, thereby strengthening capillary interactions and promoting larger bundles, whereas larger contact angles would suppress aggregation. A systematic investigation of wettability effects remains an interesting direction for the future work.

Regarding the validity range of the scaling analysis, the balance underlying Eq. (1) requires $h \ll l$. When h approaches l, the entire fin surface is wetted, and the model breaks down. Substituting the upper bound $h_{\max} \sim l$ into Eq. (4) gives a physical upper bound on the bundle size, $N_{\max} \sim (\gamma w l^4/Bs^2)^{1/3}$, beyond which the scaling is no longer expected to hold. This design-limited saturation is consistent with the plateau observed at the highest withdrawal speeds in Figs. 1(c) and 3(d). We also note that the maximum reliable operating speed of the motorized linear stage is approximately 0.4 m/s, although the saturation plateau is already fully established well below this limit, so the accessible speed window is sufficient to identify the saturation behavior.

These results highlight the central role of dynamic meniscus formation in governing elastocapillary aggregation under withdrawal conditions and establish withdrawal speed as a tunable parameter for controlling capillary-driven assembly of deformable solids. The quantitative frameworks developed here provide general design guidelines for controlling bundle morphology in liquid-interface-driven systems, with direct implications for dip-coating of fibrous media, MEMS fabrication, and capillary-driven self-assembly of micro- and nanostructures. In dip-coating applications, operating in the quasi-static regime ($u < u_c$) can help suppress capillary-induced aggregation and promote more uniform coatings, while operating in the dynamic regime enables the deliberate formation of hierarchical bundle structures with controllable characteristic length scales. In MEMS fabrication, where structural collapse during drying is a critical concern, reducing the withdrawal speed below u_c provides an effective strategy to suppress elastocapillary aggregation and prevent undesired coalescence of neighboring microstructures. In capillary-driven self-assembly of nanostructures, the withdrawal speed can be used to tune the bundle size and hence the spatial periodicity of the assembled pattern, offering a new handle for morphology control.

This work was supported by the National Research Foundation of Korea (NRF) grants funded by the Korea government (Nos. RS-2024-00341444 and RS-2025-00564724).

AUTHOR DECLARATIONS

Conflict of Interest

The authors have no conflicts to disclose.

Author Contributions

Chan Jin Park and Youngsin Jo contributed equally to this work.

Chan Jin Park: Investigation (equal); Writing – original draft (equal); Writing – review & editing (equal). **Youngsin Jo:** Data curation (equal); Visualization (equal). **Seokmin Moon:** Conceptualization (equal); Investigation (equal). **Jonghyun Ha:** Project administration (lead); Writing – original draft (equal); Writing – review & editing (equal).

DATA AVAILABILITY

The data that support the findings of this study are available from the corresponding author upon reasonable request.

REFERENCES

[1]J. Bico, B. Roman, L. Moulin, and A. Boudaoud, "Elastocapillary coalescence in wet hair," Nature **432**, 690 (2004).
[2]H.-Y. Kim and L. Mahadevan, "Capillary rise between elastic sheets," J. Fluid Mech. **548**, 141 (2006).
[3]J. Ha and H.-Y. Kim, "Capillarity in soft porous solids," Annu. Rev. Fluid Mech. **52**, 263 (2020).
[4]J.-L. Liu and X.-Q. Feng, "On elastocapillarity: A review," Acta Mech. Sin. **28**, 928 (2012).
[5]C. Py, R. Bastien, J. Bico, B. Roman, and A. Boudaoud, "3D aggregation of wet fibers," Europhys. Lett. **77**, 44005 (2007).
[6]M. De Volder and A. J. Hart, "Engineering hierarchical nanostructures by elastocapillary self-assembly," Angew. Chem., Int. Ed. **52**, 2412 (2013).
[7]S. Gernay, W. Federle, P. Lambert, and T. Gilet, "Elasto-capillarity in insect fibrillar adhesion," J. R. Soc. Interface **13**, 20160371 (2016).
[8]A. Nasto, M. Regli, P.-T. Brun, J. Alvarado, C. Clanet, and A. E. Hosoi, "Air entrainment in hairy surfaces," Phys. Rev. Fluids **1**, 033905 (2016).
[9]J. W. Weisel, C. Nagaswami, and R. O. Peterson, "River otter hair structure facilitates interlocking to impede penetration of water and allow trapping of air," Can. J. Zool. **83**, 649–655 (2005).
[10]A. K. Geim, S. V. Dubonos, I. V. Grigorieva, K. S. Novoselov, A. A. Zhukov, and S. Y. Shapoval, "Microfabricated adhesive mimicking gecko foot-hair," Nat. Mater. **2**, 461 (2003).
[11]S. F. Chini and A. Amirfazli, "Understanding pattern collapse in photolithography process due to capillary forces," Langmuir **26**, 13707 (2010).
[12]I. Kim, J. Mun, W. Hwang, Y. Yang, and J. Rho, "Capillary-force-induced collapse lithography for controlled plasmonic nanogap structures," Microsyst. Nanoeng. **6**, 65 (2020).

20 July 2026 09:29:22

Published under an exclusive license by AIP Publishing

[13]T. Ghosh *et al.*, "Preventing the capillary-induced collapse of vertical nanostructures," ACS Appl. Mater. Interfaces **14**, 5537 (2022).
[14]C.-C. Chang, Z. Wang, Y.-J. Sheng, and H.-K. Tsao, "Nanostructure collapse by elasto-capillary instability," Soft Matter **10**, 8542 (2014).
[15]D. R. Biswas, "Optical fiber coatings for biomedical applications," Opt. Eng. **31**, 1400 (1992).
[16]Z. Gui, H. Zhu, E. Gillette, X. Han, G. W. Rubloff, L. Hu, and S. B. Lee, "Natural cellulose fiber as substrate for supercapacitor," ACS Nano **7**, 6037 (2013).
[17]S. Zhai *et al.*, "Textile energy storage: Structural design concepts, material selection and future perspectives," Energy Storage Mater. **3**, 123 (2016).
[18]X. Tang and X. Yan, "Dip-coating for fibrous materials: Mechanism, methods and applications," J. Sol-Gel Sci. Technol. **81**, 378 (2017).
[19]R. Wang, F. Zhao, P. Li, L. Wang, S. Tang, and J. Liu, "Paint release control of brush," AIP Adv. **11**, 015115 (2021).
[20]D. Grosso, "How to exploit the full potential of the dip-coating process to better control film formation," J. Mater. Chem. **21**, 17033 (2011).
[21]B. Pokroy, S. H. Kang, L. Mahadevan, and J. Aizenberg, "Self-organization of a mesoscale bristle into ordered, hierarchical helical assemblies," Science **323**, 237 (2009).
[22]Y. Hu *et al.*, "Laser printing hierarchical structures with the aid of controlled capillary-driven self-assembly," Proc. Natl. Acad. Sci. U. S. A. **112**, 6876 (2015).
[23]A. Kim, F. S. Ou, D. A. A. Ohlberg, M. Hu, R. S. Williams, and Z. Li, "Study of molecular trapping inside gold nanofinger arrays on surface-enhanced Raman substrates," J. Am. Chem. Soc. **133**, 8234 (2011).
[24]J.-L. Liu, X.-Q. Feng, R. Xia, and H.-P. Zhao, "Hierarchical capillary adhesion of microcantilevers or hairs," J. Phys. D **40**, 5564 (2007).
[25]A. E. Cohen and L. Mahadevan, "Kinks, rings, and rackets in filamentous structures," Proc. Natl. Acad. Sci. U. S. A. **100**, 12141 (2003).
[26]D. Quéré, "Fluid coating on a fiber," Annu. Rev. Fluid Mech. **31**, 347 (1999).
[27]W. J. Smit, C. Kusina, A. Colin, and J.-F. Joanny, "Withdrawal and dip coating of an object from a yield-stress reservoir," Phys. Rev. Fluids **6**, 063302 (2021).
[28]S. R. Bhopalam, J. Bueno, and H. Gomez, "*Fibrotaxis*: Gradient-free, spontaneous and controllable droplet motion on soft solids," Soft Matter **20**, 9301–9311 (2024).
[29]S. R. Bhopalam, R. Juanes, and H. Gomez, "Simulating fluid–fluid displacement in a soft capillary tube: How compliance delays interfacial instability and bubble pinch-off," Comput. Methods Appl. Mech. Eng. **448**, 118430 (2026).
[30]S. Moon and J. Ha, "Dynamics of fluid–structure interaction in paintbrush," Phys. Fluids **36**, 112105 (2024).
[31]H. Bense, E. Siefért, and F. Brau, "Measurement of capillary forces using two fibers dynamically withdrawn from a liquid: Evidence for an enhanced cheerios effect," Phys. Rev. Lett. **131**, 184003 (2023).
[32]J. Ha, Y. S. Kim, K. Jiang, R. Siu, and S. Tawfick, "Hydrodynamic elastocapillary morphing of hair bundles," Phys. Rev. Lett. **125**, 254503 (2020).
[33]P.-G. de Gennes, F. Brochard-Wyart, and D. Quéré, *Capillarity and Wetting Phenomena* (Springer, New York, 2004).
[34]C. A. Schneider, W. S. Rasband, and K. W. Eliceiri, "NIH image to ImageJ: 25 years of image analysis," Nat. Methods **9**, 671–675 (2012).
[35]L. Landau and B. Levich, "Dragging of a liquid by a moving plate," in *Dynamics of Curved Fronts* (Academic Press, 1988), pp. 141–153.

20 July 2026 09:29:22

Published under an exclusive license by AIP Publishing